Spin-Selective Second-Harmonic Vortex Beam Generation with Babinet-Inverted Plasmonic Metasurfaces

Yang Chen, Xiaodong Yang,* and Jie Gao*

Metasurfaces have drawn considerable attentions for their revolutionary capability of tailoring the amplitude, phase, and polarization of light. By integrating the nonlinear optical processes into metasurfaces, new wavelengths are introduced as an extra degree of freedom for further advancing the device performance. However, most of the existing nonlinear plasmonic metasurfaces are based on metallic nanoantennas as meta-atoms, suffering from strong background transmission, low laser damage threshold and small nonlinear conversion efficiency. Here, Babinet-inverted plasmonic metasurfaces made of C-shaped nanoapertures as meta-atoms are designed and demonstrated to solve these issues. Rotation-gradient nonlinear metasurfaces are further constructed for producing spin-selective second-harmonic vortex beams with the orbital angular momentum (OAM) and beam diffraction angle determined by both the spin states of the fundamental wave and second-harmonic emission. The results enable new types of functional metasurface chips for applications in spin, OAM, and wavelength multiplexed optical trapping, all-optical communication, and optical data storage.

1. Introduction

Metasurfaces consisting of flat meta-atom arrays have undergone explosive development in the past decade for their capability of arbitrarily manipulating the spatial distributions of amplitude, phase, and polarization of light at subwavelength scale in linear optics regime, enabling versatile applications such as structured beam generation, ultrathin lenses, polarization conversion, chiroptical spectroscopy, and holographic image construction.[1–13] Recently, the concept of metasurface has been extended to the nonlinear optics regime for coherent generation of nonlinear beams and local manipulation of the beam wavefront at new frequencies.[14–23] The incorporation of nonlinear optical processes into metasurfaces will introduce new wavelengths as an extra degree of freedom to further expand the functionalities of metasurface-based devices. The high intrinsic nonlinear susceptibility of metal materials (such as Au, Ag, and Al) at the metal–dielectric interface and the local field enhancement result in strong nonlinear optical responses in plasmonic metasurfaces.[24] Compared to the conventional quadratic nonlinear optical materials such as ferroelectric crystals, nonlinear plasmonic metasurfaces can continuously control the local phase shift of effective nonlinear polarizability in the entire 2π range with subwavelength resolution for nonlinear wavefront shaping.[14]

Among various applications of metasurfaces, the generation of optical vortex beam with helical wavefront carrying orbital angular momentum (OAM) has attracted great interests.[8,11,25–29] Compared to the conventional bulk optical components used for generating vortex beams, such as spatial light modulator and spiral phase plate, metasurfaces provide a compact and high-resolution approach, which open new avenues for optical particle trapping,[30,31] precision photolithography,[32,33] and remote optical communication.[34,35] Furthermore, the generation of second-harmonic (SH) vortex beams have been recently achieved with both the fork-type and rotation plasmonic metasurfaces,[19,21] but the formed SH vortex beams can only carry OAM of one absolute value and the vortex mode purity is still limited. Besides, the fork-type metasurface demonstrates no spin control over the created SH vortex pair,[19] while the rotation metasurface can only generate one vortex beam with the opposite spin at one time.[21] Moreover, most of the existing nonlinear plasmonic metasurfaces employ metallic nanoantennas as their constitutional meta-atoms, which suffer from strong background transmission, undesired optical scattering, and low laser damage threshold. As a solution, Babinet-inverted plasmonic metasurfaces based on nanoapertures in metallic film as nonlinear meta-atoms have their unique advantages, where the transmission of background illumination and undesired optical scattering can be efficiently suppressed, resulting in a significantly improved signal-to-noise ratio for the nonlinear beam conversion.[36] Meanwhile, the generated Joule heat in Babinet-inverted plasmonic metasurfaces under the femtosecond laser illumination can diffuse rapidly across the continuous metallic film with high thermal conductivity, leading to a high laser damage threshold.[37,38]

In this work, we present Babinet-inverted plasmonic metasurfaces based on C-shaped nanoapertures for achieving strong SH emission with large nonlinear conversion efficiency and generating spin-selective SH vortex beams with high mode purity. The geometrical parameters of C-shaped nanoapertures,

Dr. Y. Chen, Prof. X. Yang, Prof. J. Gao
Department of Mechanical and Aerospace Engineering
Missouri University of Science and Technology
Rolla, MO 65409, USA
E-mail: yangxia@mst.edu; gaojie@mst.edu

The ORCID identification number(s) for the author(s) of this article can be found under https://doi.org/10.1002/adom.201800646.
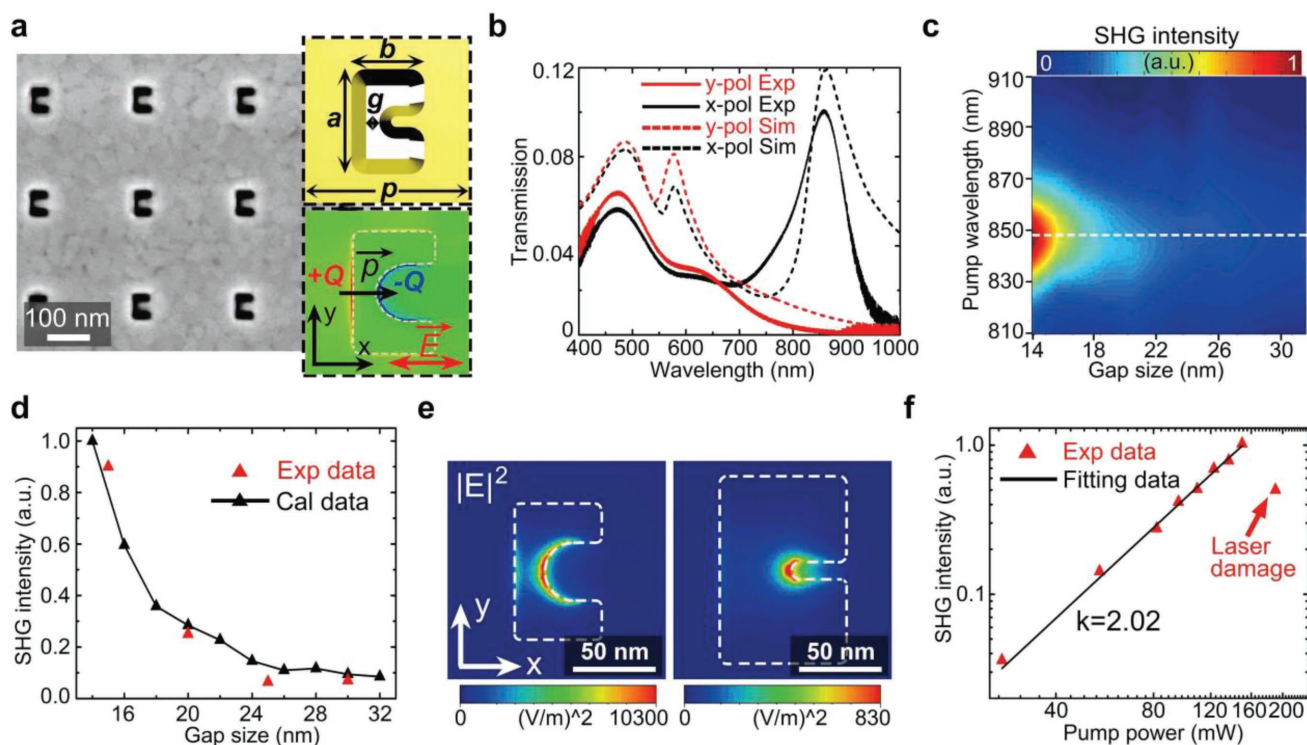
Figure 1. a) Scanning electron microscope (SEM) image of a uniform C-shaped nanoaperture array. Inset up: schematic of a single C-shaped nanoaperture with geometrical parameters marked. Inset low: illustration of the generated electric dipole across the gap. b) Experimental and simulated transmission spectra of the uniform C-shaped nanoaperture array under linear polarization basis ($a = 110$ nm, $b = 80$ nm, $g = 15$ nm, $p = 240$ nm). c) Calculated SHG intensity as a function of fundamental pump wavelength and nanoaperture gap size. d) Calculated and experimental SHG intensity depending on the nanoaperture gap size under x-polarized fundamental incidence, where the calculated data corresponds to the horizontal dashed line in (c) at the pump wavelength of 848 nm. e) Simulated near-field distributions $|E|^2$ of C-shaped nanoaperture at 848 nm (left: 2 nm below the bottom surface, right: 2 nm above the top surface). f) Log–log plot of the radiated SH power with respect to the pump power of x-polarized fundamental wave at 848 nm.

especially the gap size, are optimized to highly enhance the second-harmonic generation (SHG) signal, which is well predicted by numerical simulations according to the nonlinear scattering theory. Owing to the circularly dichroic field overlap of the optical modes in the C-shaped nanoaperture, the SH radiation under circularly polarized incidence displays a large intensity selection ratio between two output spin states. By combining the rotation phase profile with the gradient phase profile in one single nonlinear metasurface, spin-selective SH vortex beams with specified OAM values are generated and separated at different diffraction angles, depending on both the spin states of the fundamental wave and second-harmonic emission. Our demonstrated nonlinear plasmonic metasurfaces will provide a promising platform for on-chip nonlinear beam generation and manipulation, as well as spin, OAM, and wavelength multiplexed optical trapping, all-optical communications, and holographic imaging.

2. Results and Discussion

To generate strong SH radiation, Babinet-inverted C-shaped nanoapertures are selected as nonlinear meta-atoms due to their noncentrosymmetric shape and large local field enhancement. The C-shaped nanoapertures are milled in a 50 nm thick gold film deposited on a silica substrate using focused ion beam

system as shown in **Figure 1**a (see the Experimental Section). Measured and simulated transmission spectra through the uniform C-shaped nanoaperture array under linear polarization basis shown in Figure 1b indicate the pronounced optical anisotropy of the nanoaperture. Under x-polarized wave excitation, an electric dipole is formed across the nanoaperture gap where electric charges with opposite signs are accumulated on the two sides of the gap (Figure 1a). Compared to the metallic split ring resonator that possessing a magnetic dipole,[16,39] the C-shaped nanoaperture has much higher local field enhancement at the gap area.[40] The strength of the electric dipole and the resulting field enhancement is substantially increased as the gap size g gets smaller,[41–43] which can greatly boost the SH emission from the C-shaped nanoaperture in the electric dipole approximation

$$P^{(2)}(2\omega) = \chi^{(2)} : E(\omega)E(\omega) \tag{1}$$

where $P^{(2)}(2\omega)$ is the second-order polarization, $E(\omega)$ is the fundamental electric field distribution, and $\chi^{(2)}$ is the second-order nonlinear susceptibility. On the other hand, the outlined area of the C-shaped nanoaperture is reduced with the decreased gap size in order to maintain the electric dipole resonance unchanged, leading to a lower transmission (Figure S1, Supporting Information). In order to evaluate the influence of the gap size g on the SHG intensity, numerical simulation

ADVANCED
SCIENCE NEWS
www.advancedsciencenews.com

ADVANCED
OPTICAL
MATERIALS
www.advopticalmat.de

based on the nonlinear scattering theory[44–46] is conducted (Figure S2, Supporting Information). The electric field amplitude of the SH radiation $E_{SH}(2\omega)$ is estimated as

$$E_{SH}(2\omega) \propto \iint (\chi_{nnn} E'_n(2\omega) E_n^2(\omega) + \chi_{ntt} E'_n(2\omega) E_t^2(\omega) \\ + \chi_{ttn} E'_t(2\omega) E_t(\omega) E_n(\omega)) \, dS \quad (2)$$

where $E(\omega)$ is the electric field at the fundamental wavelength and $E'(2\omega)$ is the electric field under a time-reversed incidence at the SH wavelength. The subscript n or t denotes the direction normal or transverse to the surface. χ_{nnn}, χ_{ntt}, χ_{ttn} are the second-order nonlinear susceptibilities of gold. Calculation results in Figure 1c validate that the SH emission under x-polarized fundamental incidence is significantly boosted by employing a smaller gap size, which matches well with the experimental results in Figure 1d. Therefore, C-shaped nanoapertures are designed to have a gap size of 15 nm, which is about the minimum feature size milled with the focused ion beam system. Besides, the maximum SHG is achieved under the pump wavelength of 848 nm that is slightly blueshifted relative to the electric dipole resonance at 860 nm. At 848 nm, electric field intensity enhancement can be up to 1.03×10^4 near the bottom surface as depicted in Figure 1e. Even at the top surface

where the gap is greatly enlarged due to the tapered sidewall, a large intensity enhancement of 830 is still achieved. As presented in Figure 1f, the dependence of the emitted SH power on the pump power of x-polarized fundamental wave is measured and fitted to be quadratic. The maximum SHG intensity is produced under the pump power of 150 mW, corresponding to a power density of 5.3 kW cm^{-2}, above which heat damage starts to come into play (Figure S3, Supporting Information). The laser damage threshold is dramatically elevated for nanoapertures compared to nanoantennas under femtosecond laser illumination, benefitting from the rapid heat diffusion across the continuous gold film with high thermal conductivity. The SHG conversion efficiency at wavelength of 848 nm is up to 3.2×10^{-9}, which is several times larger than the previously published results.[19,47,48]

In order to shape the wavefront of the fundamental beam and the generated SH beam, C-shaped nanoapertures are employed as Pancharatnam–Berry optical elements (PBOEs) operating in both linear and nonlinear regimes as illustrated in **Figure 2**a.[14,49] For the C-shaped nanoaperture with an orientation angle φ, the circularly polarized incident beam with original spin σ is partially converted to the cross-polarized spin $-\sigma$ accompanied by a geometric phase of 2φ due to the high polarization anisotropy of the nanoaperture. The unconverted
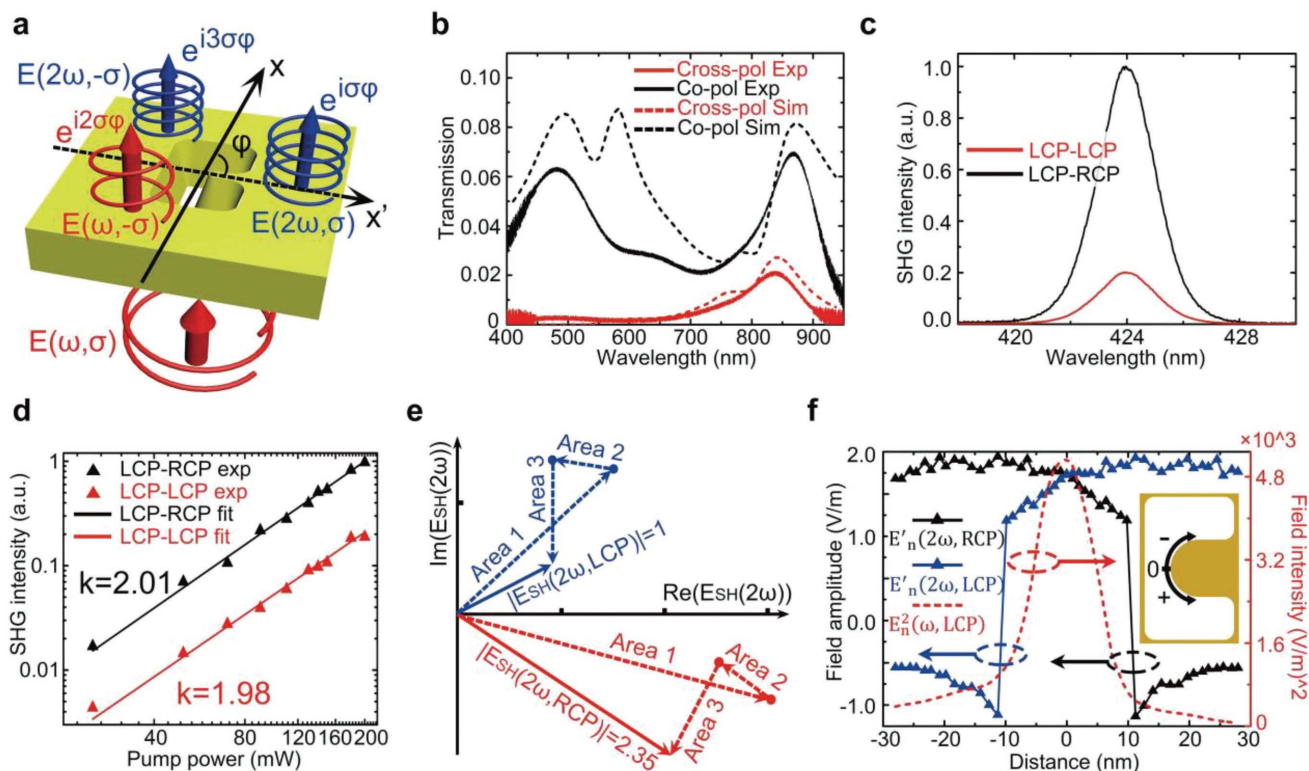

Figure 2. a) Illustration of the linear and nonlinear geometric phases introduced under circular polarization. b) Experimental and simulated transmission spectra of the uniform C-shaped nanoaperture array under circular polarization basis. c) Measured SHG intensity of left-handed and right-handed circular polarized (LCP and RCP) components under LCP fundamental incidence of 200 mW at 848 nm. d) Log–log plot of the output SHG intensity of LCP and RCP components as a function of the pump power of LCP fundamental wave at 848 nm. e) Normalized complex values of the surface integrals over three surface areas of the C-shaped nanoaperture for the generated LCP and RCP SH emission under LCP fundamental incidence (area 1: sidewall, area 2: top surface, area 3: bottom surface). f) Electric field distributions of $E'_n(2\omega, RCP)$, $E'_n(2\omega, LCP)$, and $E_n^2(\omega, LCP)$ along the gap ridge path shown in the inset at the plane 5 nm above the bottom surface at the fundamental wavelength of 848 nm, where the positive field amplitude represents the field direction pointing out of the metal surface.

**ADVANCED
SCIENCE NEWS**
www.advancedsciencenews.com

**ADVANCED
OPTICAL
MATERIALS**
www.advopticalmat.de

fundamental beam component with the copolarized spin σ does not carry any geometric phase information. Meanwhile, the two generated SH beam components with the copolarized spin σ and the cross-polarized spin $-\sigma$ from the C-shaped nanoaperture obtain a geometric phases of φ and 3φ, respectively, which originates from the onefold rotational symmetry of the nanoaperture following the selection rules for SHG under circular polarization.[50,51]

When the C-shaped nanoapertures are utilized as linear PBOEs, the transmission of the cross-polarized component is much lower than that of the copolarized component due to the low birefringent phase retardation (Figure 2b). On the contrary, when the C-shaped nanoapertures operate in the nonlinear regime, the measured SHG intensity of the cross-polarized spin is 5.02 times stronger than that of the copolarized spin σ under the pump power of 200 mW (Figure 2c). Note that the laser damage threshold under circularly polarized wave is larger than that under x-polarized wave for the optical anisotropy. The SHG intensity of each spin component follows a quadratic dependence on the fundamental pump power (Figure 2d). It is not expected that the C-shaped nanoaperture with onefold rotational symmetry can achieve such a high SHG intensity selection ratio over the spin state, which is usually realized by using nanostructures with threefold rotational symmetry according to the selection rules for SHG.[21,52] In order to reveal the underlying mechanism, numerical simulations based on the nonlinear scattering theory are adopted under circular polarization basis.[46,52] The calculated SHG intensity selection ratio defined as $I(2\omega, RCP)/I(2\omega, LCP)$ is 5.52 (equivalent to the amplitude ratio of 2.35) under LCP fundamental illumination, which agrees well with the measured value of 5.02. According to the nonlinear scattering theory, the complex-valued microscopic contributions from all three surface areas of the C-shaped nanoaperture, including sidewall, top surface, and bottom surface, will add up to form the net nonlinear emission. The surface integral of $E_{SH}(2\omega)$ in Equation (2) over the three

surface areas is then plotted in a complex plane representation as shown in Figure 2e. It is observed that the sum vector of the cross-polarized spin (RCP) is around 2.35 times stronger than that of the copolarized spin (LCP), where the difference mainly comes from the larger surface integral over the sidewall area for the RCP SH emission, as well as much more destructive interference from different surface areas for the LCP SH emission. To go a step further, field overlap conditions between the optical modes of $E(\omega)$ and $E'(2\omega)$ are investigated by evaluating the normal components of electric fields $E_n^2(\omega, LCP)$, $E'_n(2\omega, LCP)$, and $E'_n(2\omega, RCP)$ along the gap ridge at the fundamental wavelength of 848 nm, because the optical near field is mostly enhanced in this area and $\chi_{nnn}E'_n(2\omega)E_n^2(\omega)$ is the dominant term in the surface integral of $E_{SH}(2\omega)$. As shown in Figure 2f, $E'_n(2\omega, RCP)$ is mainly confined at the upper half of the gap ridge and it changes its direction at the lower half, while $E'_n(2\omega, LCP)$ exhibit a mirror-symmetric distribution with $E'_n(2\omega, RCP)$. Meanwhile, $E_n^2(\omega, LCP)$ manifests an asymmetric distribution around the gap ridge with slightly higher intensity at the upper half, resulting in a better field overlap with $E'_n(2\omega, RCP)$ in comparison to $E'_n(2\omega, LCP)$.

The rotation nonlinear metasurface is constructed with C-shaped nanoapertures arranged at the position-dependent orientation angles of $\varphi = a\tan 2 (x/y)$ within the interval of $-\pi$ and π (**Figure 3**a). To capture the generated SH images, an electron-multiplying charge-coupled device (EMCCD) is used for its high photonic sensitivity. In addition, a color CCD is also applied in the measurements, benefitting from the strong SH radiation signal and high signal-to-noise ratio enabled by the C-shaped nanoapertures (Figure S4, Supporting Information). By illuminating the rotation metasurface vertically with an LCP fundamental Gaussian beam at 848 nm, three different spiral phase fronts carrying OAM of $+2\hbar$, $+1\hbar$, and $+3\hbar$ are formed right behind the metasurface for the transmitted RCP fundamental beam, the LCP SH beam and the RCP SH beam, respectively. Consequently, three linear and nonlinear vortex beams with
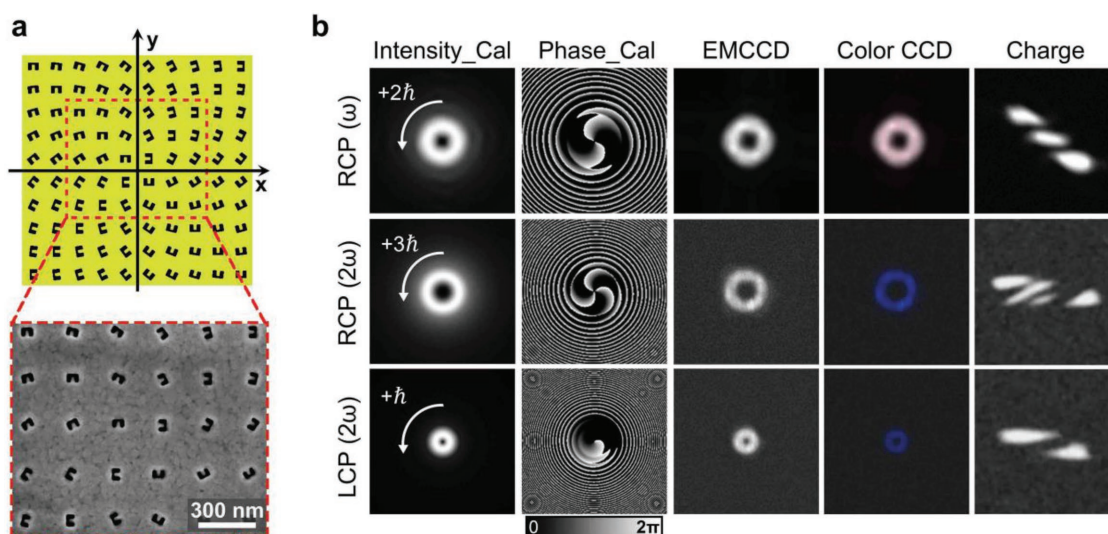

Figure 3. a) Schematic and SEM image of the rotation nonlinear metasurface made of C-shaped nanoapertures. b) Calculated intensity distributions (Intensity_Cal) and phase distributions (Phase_Cal), captured EMCCD images and color CCD images, and measured topological charge images of the generated fundamental and SH vortex beams under LCP fundamental incidence.

ADVANCED
SCIENCE NEWS
www.advancedsciencenews.com

ADVANCED
OPTICAL
MATERIALS
www.advopticalmat.de

donut-shaped intensity profiles are generated in the far-field as calculated and measured in Figure 3b (see the Experimental Section). Their topological charges are examined and validated by counting the dark stripes of the images converted by a cylindrical lens.[53] Owing to the nanoaperture meta-atoms, background illumination and other undesired scattering from the metasurface sample are effectively suppressed, resulting in much clearer nonlinear beam images compared to other works.[11,25,26] It is observed that the generated SH vortex beam with RCP spin has an ring radius approximately twice as that of LCP spin due to the different OAM values,[54] while the ring radius of the fundamental vortex beam is bigger than the two SH vortex beams due to the doubled wavelength. If the input and output beams change their handedness simultaneously, the corresponding vortex beam will possess the reversed OAM value with its essential intensity profiles maintained (Figure S5, Supporting Information). The imperfections of the measured donut-like beam shape are mainly attributed to the optical disalignment, the sample fabrication tolerance, and the non-Gaussian profile of incident beam.

The generated SH vortex beams are usually impure and mixed with other undesired SHG components, such as the SH emission of the opposite spin and the SH scattering from the imperfections of metasurface. To overcome this problem, the rotation-gradient nonlinear metasurface combining the spiral phase profile and linear gradient phase profile is constructed to produce SH vortex beams along specified diffraction directions in order to separate them from the disturbing components.[11] Furthermore, the rotation-gradient metasurface also enables the generation of multiple vortex beams with different beam properties simultaneously. As shown in **Figure 4**a, the orientation angles of C-shaped nanoapertures in the rotation-gradient array is expressed as $\phi = a\tan2(x/y) + x \cdot \theta$, where $\theta = 30°$ is the constant angle gradient along the horizontal direction. The deflection angle ψ of a generated SH vortex beam is determined by

$$\psi = a\tan\left(\frac{(2\sigma_{FF} - \sigma_{SH}) \cdot \theta \cdot \lambda_{SH}}{2\pi \cdot p}\right) \quad (3)$$
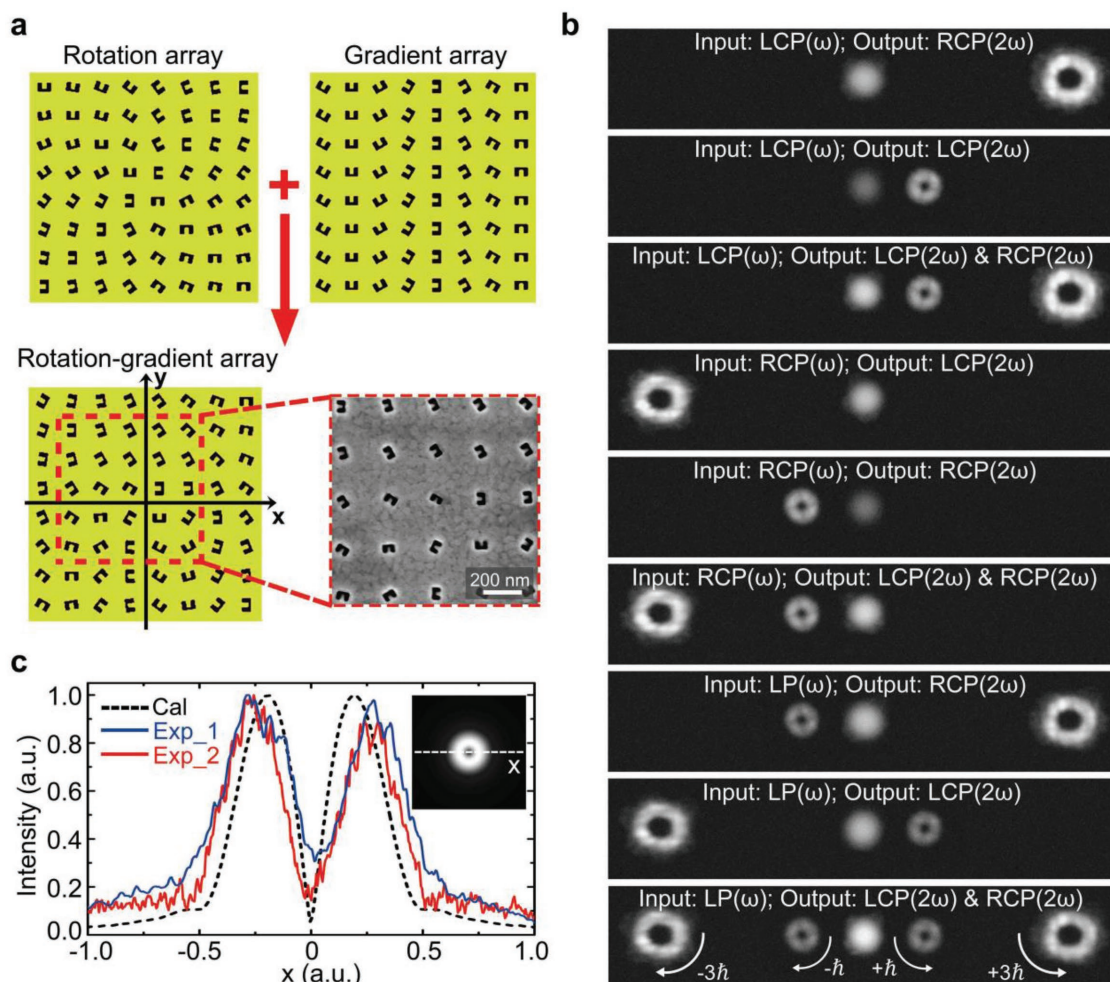

Figure 4. a) Schematic of the transformation process of rotation-gradient C-shaped nanoaperture array and its SEM image. b) Captured EMCCD images of the spin-selective SH vortex beams produced and separated by the rotation-gradient metasurface. c) Optical intensity distributions along the central cutline of one generated SH vortex beam (Input: LCP(ω); Output: LCP(2ω)) from calculation (Cal), rotation metasurface (Exp_1) and rotation-gradient metasurface (Exp_2).
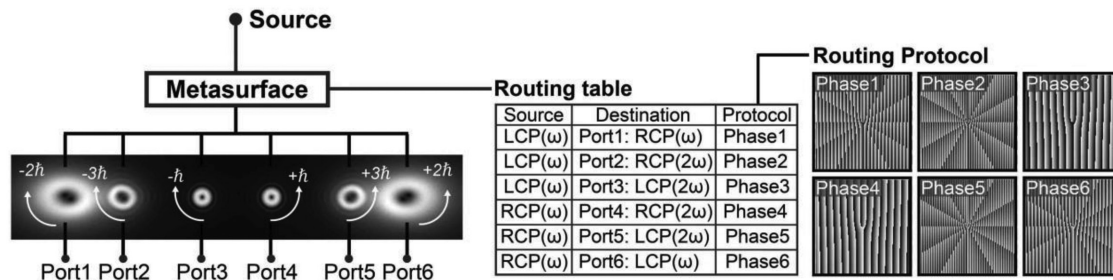
Figure 5. Illustration of the rotation-gradient nonlinear metasurface serving as an all-optical router.

where p is the unit cell period and λ_{SH} is the second-harmonic wavelength. σ_{FF} and σ_{SH} indicate the spin states of the incident fundamental beam and the radiated SH beam, which is equal to +1 or −1 for LCP or RCP. Under LCP fundamental incidence at 848 nm, two SH vortex beams with RCP and LCP possessing OAM of $+3\hbar$ and $+1\hbar$ are diffracted to the right side with deflection angles of 23.7° and 8.3°, respectively (Figure 4b). Under RCP fundamental beam illumination, two vortex beams with OAM of $-3\hbar$ and $-\hbar$ are deflected to the left side for the LCP and RCP components due to the inverted geometric phase profiles. Under linear polarized fundamental incidence, up to four SH vortex beams are simultaneously produced and separated by the rotation-gradient metasurface with OAM of $\pm1\hbar$ and $\pm3\hbar$. In order to illustrate the improvement of vortex mode purity enabled by the rotation-gradient nonlinear metasurface, optical intensity distributions across the center of one generated SH vortex beam are compared in Figure 4c. Theoretically, the optical intensity should be nearly zero at the vortex beam center due to the phase singularity. This feature is much better represented by the SH vortex beam created from the rotation-gradient metasurface, which suggests the higher mode purity, rather than the rotation metasurface.

The proposed rotation-gradient nonlinear metasurfaces offer a promising integrated platform for many applications, such as spin, OAM, and wavelength multiplexed all-optical communications. As illustrated in **Figure 5**, the metasurface can serve as a six-channel on-chip all-optical router. The routing table listing the routes to particular network destinations is encoded in the nonlinear metasurface to load different phase modulations (routing protocol) on the input fundamental beam signal according to its spin state and then route the input signal to distinct output ports with specified spin states, OAM values, and wavelengths. Besides, the signal power of the four SH ports (Port 2 to Port 5) is substantially weaker than that of the two fundamental ports (Port 1 and Port 6), which can be utilized for signal encryption. Moreover, the signals from the six output ports possess distinguished optical properties in spin state, OAM, and wavelength, which are ready for the subsequent signal processing using polarizers or band-pass filters.

3. Conclusion

In summary, we have demonstrated the unprecedented capacity of Babinet-inverted plasmonic metasurfaces constructed from C-shaped nanoapertures to achieve large SHG nonlinear conversion efficiency and produce multiple SH vortex beams with high mode purity simultaneously along separated diffraction directions. The generated spin-selective SH vortex beams carry different OAM values depending on both the spin states of the incident fundamental beam and the output SH emission. Benefiting from the nanoaperture meta-atoms, the proposed nonlinear metasurfaces also exhibit improved signal-to-noise ratio and high laser damage threshold. Numerical simulations based on the nonlinear scattering theory have been utilized to optimize the enhanced SH emission from the C-shaped nanoaperture and reveal the large SHG intensity selection ratio over the spin state. This new type of nonlinear metasurfaces promise many exciting applications in structured nonlinear beam conversion, holographic imaging, all-optical communications, and optical encryption.

4. Experimental Section

Metasurface Fabrication: A 50 nm thick gold film was deposited on a silica substrate using electron-beam evaporation. Then the designed C-shaped nanoaperture arrays were milled in the gold film using focused ion beam system (FEI Helios Nanolab 600, 30 kV, 1.1 pA). The focus and astigmatism of the ion beam were carefully optimized to ensure the uniformity of C-shaped nanoapertures during the fabrication. The ion dose was accurately controlled to maintain a constant 15 nm gap size for each C-shaped nanoaperture.

Simulation and Calculation Method: The linear optical response of the C-shaped nanoaperture was simulated by using the finite element solver COMSOL Multiphysics. The permittivity of gold was obtained from spectroscopic ellipsometry data fitted with a general oscillator model and the refractive index of silica substrate is set as 1.45. Periodic boundary conditions were employed at the x and y directions and perfectly matched layers surrounded by scattering boundary condition were applied along the propagation direction.

For estimating the SH emission based on the nonlinear scattering theory, the nanoaperture was first excited with a plane wave at the fundamental pump wavelength to simulate the electric field distribution of $E_n^2(\omega)$. Then another simulation was performed with a second plane wave coming from the detector at the SH wavelength to calculate the electric field distribution of $E'_n(2\omega)$ under certain polarization. Near-field distributions on the metallic surface were then extracted from the two simulations and brought into Equation (2) to calculate the surface integral for $E_{SH}(2\omega)$. The nonlinear susceptibilities of gold were $\chi_{nnn} = 4.42 \times 10^{-22}$ m^2 V^{-1}, $\chi_{ntt} = 4.94 \times 10^{-21}$ m^2 V^{-1}, $\chi_{ttn} = 1.77 \times 10^{-21}$ m^2 V^{-1}.[55]

In order to calculating the intensity and phase profiles of the generated fundamental and SH vortex beams, the Fresnel-Kirchhoff equation is used

$$U(x,y,z) = \frac{1}{j\lambda} \iint U_0(x_0,y_0,z_0) \frac{\exp(jkr)}{r} dx_0 dy_0 \qquad (4)$$

where $U_0(x_0, y_0, z_0)$ and $U(x, y, z)$ are the complex field distributions at the metasurface plane and the image plane, respectively, $k = 2\pi/\lambda$ is the wavevector and $r = \sqrt{(x_0 - x)^2 + (y_0 - y)^2 + (z_0 - z)^2}$ is the distance between two points on the metasurface plane and the image plane. On the metasurface plane, the amplitude field follows a Gaussian distribution, and the phase field is acquired according to the local geometric phases introduced by the oriented nanoaperture meta-atoms. The intensity selection ratio of the output SH emission between two spin states is taken into account when setting the amplitude field.

Optical Characterization Setup: As illustrated in Figure S4 of the Supporting Information, femtosecond laser pulse at the fundamental wavelength from an ultrafast Ti:sapphire oscillator (Spectra-Physics Tsunami, pulse width <100 fs, repetition rate 80 MHz) is slightly focused onto the metasurface through an achromatic lens ($f = 35$ mm) with a spot size diameter of about 60 µm. An average pump power of 30 and 200 mW (measured in front of the sample) is used for the generation of fundamental vortex beam and SH vortex beam, respectively, corresponding to a pump power density of ≈1.06 kW and ≈7.07 kW cm^{-2}. Linear and nonlinear transmission images are collected by a 20× objective (NA = 0.42) and guided to a color CCD or an EMCCD (Andor iXon Ultra). By inserting or removing a short-pass filter and a band-pass filter, CCD images of the fundamental or SH vortex beams are captured. Optical intensity and spectrum of the SH radiation from the metasurface are measured by a spectrometer (Horiba, iHR 550).

Supporting Information

Supporting Information is available from the Wiley Online Library or from the author.

Conflict of Interest

The authors declare no conflict of interest.

[1] N. Yu, P. Genevet, M. A. Kats, F. Aieta, J. P. Tetienne, F. Capasso, Z. Gaburro, *Science* **2011**, *334*, 333.

[2] X. Ni, N. K. Emani, A. V. Kildishev, A. Boltasseva, V. M. Shalaev, *Science* **2012**, *335*, 427.

[3] F. Aieta, P. Genevet, M. A. Kats, N. Yu, R. Blanchard, Z. Gaburro, F. Capasso, *Nano Lett.* **2012**, *12*, 4932.

[4] W. T. Chen, K. Y. Yang, C. M. Wang, Y. W. Huang, G. Sun, I. D. Chiang, C. Y. Liao, W. L. Hsu, H. T. Lin, S. Sun, L. Zhou, A. Q. Liu, D. P. Tsai, *Nano Lett.* **2014**, *14*, 225.

[5] K. Huang, H. Liu, F. J. Garcia-Vidal, M. Hong, B. Luk'yanchuk, J. Teng, C. W. Qiu, *Nat. Commun.* **2015**, *6*, 7059.

[6] Z. Li, E. Palacios, S. Butun, K. Aydin, *Nano Lett.* **2015**, *15*, 1615.

[7] Z. Liu, Z. Li, Z. Liu, J. Li, H. Cheng, P. Yu, W. Liu, C. Tang, C. Gu, J. Li, S. Chen, J. Tian, *Adv. Funct. Mater.* **2015**, *25*, 5428.

[8] J. Zeng, J. Gao, T. S. Luk, N. M. Litchinitser, X. Yang, *Nano Lett.* **2015**, *15*, 5363.

[9] E. Maguid, I. Yulevich, D. Veksler, V. Kleiner, M. L. Brongersma, E. Hasman, *Science* **2016**, *352*, 1202.

[10] R. C. Devlin, M. Khorasaninejad, W. T. Chen, J. Oh, F. Capasso, *Proc. Natl. Acad. Sci. USA* **2016**, *113*, 10473.

[11] J. Zeng, L. Li, X. Yang, J. Gao, *Nano Lett.* **2016**, *16*, 3101.

[12] W. Wan, J. Gao, X. Yang, *ACS Nano* **2016**, *10*, 10671.

[13] Y. Chen, J. Gao, X. Yang, *Nano Lett.* **2018**, *18*, 520.

[14] G. Li, S. Chen, N. Pholchai, B. Reineke, P. W. Wong, E. Y. Pun, K. W. Cheah, T. Zentgraf, S. Zhang, *Nat. Mater.* **2015**, *14*, 607.

[15] O. Wolf, S. Campione, A. Benz, A. P. Ravikumar, S. Liu, T. S. Luk, E. A. Kadlec, E. A. Shaner, J. F. Klem, M. B. Sinclair, I. Brener, *Nat. Commun.* **2015**, *6*, 7667.

[16] N. Segal, S. Keren-Zur, N. Hendler, T. Ellenbogen, *Nat. Photonics* **2015**, *9*, 180.

[17] W. Ye, F. Zeuner, X. Li, B. Reineke, S. He, C. W. Qiu, J. Liu, Y. Wang, S. Zhang, T. Zentgraf, *Nat. Commun.* **2016**, *7*, 11930.

[18] E. Almeida, O. Bitton, Y. Prior, *Nat. Commun.* **2016**, *7*, 12533.

[19] S. Keren-Zur, O. Avayu, L. Michaeli, T. Ellenbogen, *ACS Photonics* **2016**, *3*, 117.

[20] F. Walter, G. Li, C. Meier, S. Zhang, T. Zentgraf, *Nano Lett.* **2017**, *17*, 3171.

[21] G. Li, L. Wu, K. F. Li, S. Chen, C. Schlickriede, Z. Xu, S. Huang, W. Li, Y. Liu, E. Y. B. Pun, T. Zentgraf, K. W. Cheah, Y. Luo, S. Zhang, *Nano Lett.* **2017**, *17*, 7974.

[22] G. Li, S. Zhang, T. Zentgraf, *Nat. Rev. Mater.* **2017**, *2*, 17010.

[23] S. Keren-Zur, L. Michaeli, H. Suchowski, T. Ellenbogen, *Adv. Opt. Photonics* **2018**, *10*, 309.

[24] J. Butet, P. F. Brevet, O. J. Martin, *ACS Nano* **2015**, *9*, 10545.

[25] L. Huang, X. Chen, H. Muhlenbernd, G. Li, B. Bai, Q. Tan, G. Jin, T. Zentgraf, S. Zhang, *Nano Lett.* **2012**, *12*, 5750.

[26] Y. Yang, W. Wang, P. Moitra, I. I. Kravchenko, D. P. Briggs, J. Valentine, *Nano Lett.* **2014**, *14*, 1394.

[27] F. Yue, D. Wen, J. Xin, B. D. Gerardot, J. Li, X. Chen, *ACS Photonics* **2016**, *3*, 1558.

[28] L. Zhang, S. Liu, L. Li, T. J. Cui, *ACS Appl. Mater. Interfaces* **2017**, *9*, 36447.

[29] F. Yue, D. Wen, C. Zhang, B. D. Gerardot, W. Wang, S. Zhang, X. Chen, *Adv. Mater.* **2017**, *29*, 1603838.

[30] M. Padgett, R. Bowman, *Nat. Photonics* **2011**, *5*, 343.

[31] H. He, M. Friese, N. Heckenberg, H. Rubinsztein-Dunlop, *Phys. Rev. Lett.* **1995**, *75*, 826.

[32] R. Dorn, S. Quabis, G. Leuchs, *Phys. Rev. Lett.* **2003**, *91*, 233901.

[33] T. Bauer, S. Orlov, U. Peschel, P. Banzer, G. Leuchs, *Nat. Photonics* **2014**, *8*, 23.

[34] V. D'Ambrosio, E. Nagali, S. Walborn, L. Aolita, S. Slussarenko, L. Marrucci, F. Sciarrino, *Nat. Commun.* **2012**, *3*, 961.

[35] G. Vallone, V. D'Ambrosio, A. Sponselli, S. Slussarenko, L. Marrucci, F. Sciarrino, P. Villoresi, *Phys. Rev. Lett.* **2014**, *113*, 060503.

[36] X. Ni, S. Ishii, A. V. Kildishev, V. M. Shalaev, *Light: Sci. Appl.* **2013**, *2*, e72.

[37] P. Melentiev, T. Konstantinova, A. Afanasiev, A. Kuzin, A. Baturin, A. Tausenev, A. Konyaschenko, V. Balykin, *Laser Phys. Lett.* **2013**, *10*, 075901.

[38] P. N. Melentiev, A. E. Afanasiev, A. A. Kuzin, A. S. Baturin, V. I. Balykin, *Opt. Express* **2013**, *21*, 13896.

[39] M. W. Klein, C. Enkrich, M. Wegener, S. Linden, *Science* **2006**, *313*, 502.

[40] X. L. Shi, L. Hesselink, R. L. Thornton, *Opt. Lett.* **2003**, *28*, 1320.

[41] Z. Dong, M. Asbahi, J. Lin, D. Zhu, Y. M. Wang, K. Hippalgaonkar, H. S. Chu, W. P. Goh, F. Wang, Z. Huang, J. K. Yang, *Nano Lett.* **2015**, *15*, 5976.

[42] S. Shen, L. Meng, Y. Zhang, J. Han, Z. Ma, S. Hu, Y. He, J. Li, B. Ren, T. M. Shih, Z. Wang, Z. Yang, Z. Tian, *Nano Lett.* **2015**, *15*, 6716.

[43] S. Zhang, G. C. Li, Y. Chen, X. Zhu, S. D. Liu, D. Y. Lei, H. Duan, *ACS Nano* **2016**, *10*, 11105.

[44] S. Roke, M. Bonn, A. V. Petukhov, *Phys. Rev. B* **2004**, *70*, 115106.

[45] A. G. de Beer, S. Roke, *Phys. Rev. B* **2009**, *79*, 155420.

[46] K. O'Brien, H. Suchowski, J. Rho, A. Salandrino, B. Kante, X. Yin, X. Zhang, *Nat. Mater.* **2015**, *14*, 379.

[47] M. W. Klein, M. Wegener, N. Feth, S. Linden, *Opt. Express* **2007**, *15*, 5238.

[48] N. Feth, S. Linden, M. W. Klein, M. Decker, F. B. Niesler, Y. Zeng, W. Hoyer, J. Liu, S. W. Koch, J. V. Moloney, M. Wegener, *Opt. Lett.* **2008**, *33*, 1975.

[49] M. V. Berry, *J. Mod. Opt.* **1987**, *34*, 1401.

[50] M. Finazzi, P. Biagioni, M. Celebrano, L. Duo, *Phys. Rev. B* **2007**, *76*, 125414.

[51] K. Konishi, T. Higuchi, J. Li, J. Larsson, S. Ishii, M. Kuwata-Gonokami, *Phys. Rev. Lett.* **2014**, *112*, 135502.

[52] S. Chen, F. Zeuner, M. Weismann, B. Reineke, G. Li, V. K. Valev, K. W. Cheah, N. C. Panoiu, T. Zentgraf, S. Zhang, *Adv. Mater.* **2016**, *28*, 2992.

[53] V. Denisenko, V. Shvedov, A. S. Desyatnikov, D. N. Neshev, W. Krolikowski, A. Volyar, M. Soskin, Y. S. Kivshar, *Opt. Express* **2009**, *17*, 23374.

[54] D. L. Andrews, M. Babiker, *The Angular Momentum of Light*, Cambridge University Press, Cambridge **2012**.

[55] F. X. Wang, F. J. Rodriguez, W. M. Albers, R. Ahorinta, J. E. Sipe, M. Kauranen, *Phys. Rev. B* **2009**, *80*, 233402.